

# Vibrational Recognition of Adsorption Sites for Carbon Monoxide on Platinum and Platinum-Ruthenium Surfaces

Ismaila Dabo,<sup>1</sup> Andrzej Wieckowski,<sup>2</sup> and Nicola Marzari<sup>1</sup>

<sup>1</sup>*Department of Materials Science and Engineering,*

*Massachusetts Institute of Technology, Cambridge, MA, USA*

<sup>2</sup>*Department of Chemistry, University of Illinois at Urbana-Champaign, Urbana, IL, USA*

We have studied the vibrational properties of CO adsorbed on platinum and platinum-ruthenium surfaces using density-functional perturbation theory within the Perdew-Burke-Ernzerhof generalized-gradient approximation. The calculated C–O stretching frequencies are found to be in excellent agreement with spectroscopic measurements. The frequency shifts that take place when the surface is covered with ruthenium monolayers are also correctly predicted. This agreement for both shifts and absolute vibrational frequencies is made more remarkable by the frequent failure of local and semilocal exchange-correlation functionals in predicting the stability of the different adsorption sites for CO on transition-metal surfaces. We have investigated the chemical origin of the C–O frequency shifts introducing an orbital-resolved analysis of the force and frequency density of states, and assessed the effect of donation and backdonation on the CO vibrational frequency using a GGA + molecular U approach. These findings rationalize and establish the accuracy of density-functional calculations in predicting absolute vibrational frequencies, notwithstanding the failure in determining relative adsorption energies, in the strong chemisorption regime.

## I. INTRODUCTION

Fuel cells are energy conversion systems of potentially high environmental benefit [1] that provide electricity and heat by catalytic conversion of a fuel, such as hydrogen or methanol. Despite their advantages, several technological obstacles have hindered the deployment of fuel-cell systems. For low-temperature fuel cells that use platinum as electrode material, one major limitation is CO poisoning, whereby CO occupies active sites on the platinum catalyst and prevents fuel oxidation [2]. Typically, in polymer electrolyte membrane fuel cells (PEMFCs), CO concentrations must be brought below 10–50 ppm to maintain an acceptable catalytic performance. For comparison, CO concentrations are generally on the order of thousands of ppm in reformed hydrogen fuels [3, 4]. CO poisoning is even more problematic for direct methanol fuel cells (DMFCs) since CO is always present in critical amounts as an intermediate in methanol oxidation [5].

Ruthenium islands on platinum catalysts have been shown to considerably attenuate CO poisoning [6, 7, 8], although the microscopic details of this phenomenon are not completely understood. Two main mechanisms have been proposed to explain this improved tolerance to CO. Within the bifunctional mechanism model, adsorbed OH species generated by water dissociation at the platinum/ruthenium edge promote the oxidation of CO (*the promotion effect*) [5, 7, 8, 9, 10, 11]. According to an alternative view, ruthenium modifies the electronic structure of neighboring platinum atoms, reducing their affinity for CO (*the ligand/intrinsic effect*) [5, 11]. To investigate further these mechanisms of central interest to fuel-cell technology, it is necessary to elucidate the nature of the chemical interaction between CO

and bimetallic surfaces.

In most cases, density-functional theory provides a reliable description of molecular adsorption and dissociation on transition metals [12, 13, 14, 15, 16, 17]. However, CO adsorption on transition-metal surfaces is unexpectedly problematic. Indeed, at low CO coverage, local and generalized-gradient density-functional calculations predict CO adsorption on Pt(111) to take place at the fcc site, contradicting low-temperature experiments, which unambiguously indicate atop adsorption. This well-known qualitative discrepancy (the “CO/Pt(111) puzzle”) [18] precludes an accurate description of important phenomena, such as the surface diffusion of CO adsorbates and the thermal population of CO adsorption sites. Similar qualitative errors have been reported for CO adsorbed on rhodium and copper surfaces [18, 19, 20], and a wide body of literature exists on the subject [21, 22, 23, 24, 25, 26, 27, 28, 29, 30, 31, 32].

In this work, we highlight and rationalize the accuracy of density-functional calculations in predicting the stretching frequencies of CO adsorbed on platinum and platinum-ruthenium surfaces, notwithstanding the failure in predicting the most stable adsorption site. We first present density-functional theory and density-functional perturbation theory results for the energetic, structural and vibrational properties of adsorbed CO. Second, we introduce a novel orbital-resolved force analysis to clarify the electronic origins of the C–O frequency shifts as a function of the adsorption site. Last, we rationalize the accuracy of the stretching-frequency predictions by analyzing the influence of donation and backdonation using a GGA + molecular U model recently introduced by Kresse, Gil, and Sautet [21].

## II. THEORETICAL BASIS

The (111) transition-metal surface is modeled using a periodically repeated slab composed of four layers, each layer containing four atoms per supercell. A  $\sqrt{3} \times 2$  adsorption structure corresponding to a coverage of 1/4 of the monolayer (ML) is adopted for the CO overlayer. Atomic cores are represented by ultrasoft pseudopotentials [33]. The exchange-correlation energy is calculated within the Perdew-Burke-Ernzerhof generalized-gradient approximation (PBE-GGA) [34]. The size of the vacuum region separating the periodic slabs is  $\sim 13$  Å. We use a shifted  $4 \times 4 \times 1$  mesh with cold-smearing occupations [35] (smearing temperature of 0.4 eV) to sample the Brillouin zone. Energy cutoffs of 24 and 192 Ry are applied to the plane-wave expansions of the wavefunctions and charge density, respectively. As discussed in Ref. [18], the system is not spin-polarized. Using the above slab thickness and calculation parameters, we verify that the adsorption energies are converged within less than 10 meV and the atomic forces within a few meV/Å.

The bond length and stretching frequency of CO in the gas phase are calculated to be 1.140 Å and 2140  $\text{cm}^{-1}$  (experimental values are 1.128 Å and 2170  $\text{cm}^{-1}$ ). The PBE-GGA lattice parameter and bulk modulus of platinum are 3.993 Å and 2.36 Mbar, in good agreement with experimental values of 3.923 Å and 2.30 Mbar [36]. All our calculations use fully relaxed configurations.

site	atop	bridge	hcp	fcc
$E_{\text{ads}}$ (eV)	1.61 (1.30) <sup>b</sup>	1.71	1.72	1.74
$d(\text{C-O})$ (Å)	1.153 (1.15±0.05) <sup>c</sup>	1.177 (1.15±0.05) <sup>c</sup>	1.188	1.189
$d(\text{M-C})$ (Å)	1.864 (1.85±0.1) <sup>c</sup>	2.029 (2.08±0.07) <sup>c</sup>	2.116	2.121
$h(\text{C})$ (Å) <sup>a</sup>	2.017	1.543	1.380	1.373
$\theta(\text{CO})$ (deg) <sup>a</sup>	1.4	1.4	0.5	0.4
$\nu(\text{C-O})$ (cm <sup>-1</sup> )	2050 (2070) <sup>d</sup>	1845 (1880) <sup>d</sup>	1752 (1760) <sup>d</sup>	1743 (1760) <sup>d</sup>
$\nu(\text{M-C})$ (cm <sup>-1</sup> )	584 (470) <sup>e</sup>	413 (380) <sup>e</sup>	358	344
bending modes (cm <sup>-1</sup> )	392 386	393 346	329 315	328 300
other modes (cm <sup>-1</sup> )	0 to 230	0 to 231	0 to 196	0 to 186

<sup>a</sup> $h(\text{C})$  denotes the distance from C to the first surface layer, and  $\theta(\text{CO})$  denotes the tilt angle of CO. <sup>b</sup>Ref. [37].  
<sup>c</sup>Ref. [38]. <sup>d</sup>Ref. [39]. <sup>e</sup>Ref. [40].

TABLE I: Adsorption energies, structural properties, and vibrational frequencies calculated using density-functional theory and density-functional perturbation theory for CO adsorbed on clean Pt(111) surfaces.

site	atop	hcp	fcc	atop	hcp	fcc
slab	1 ML Ru/ 3 ML Pt	1 ML Ru/ 3 ML Pt	1 ML Ru/ 3 ML Pt	2 ML Ru/ 2 ML Pt	2 ML Ru/ 2 ML Pt	2 ML Ru/ 2 ML Pt
$E_{\text{ads}}$ (eV)	2.24	2.27	2.15	1.96	2.05	1.88
$d(\text{C-O})$ (Å)	1.161	1.196	1.192	1.161	1.201	1.190
$d(\text{M-C})$ (Å)	1.892	2.132	2.104	1.922	2.122	2.111
$h(\text{C})$ (Å) <sup>a</sup>	2.014	1.375	1.412	1.970	1.318	1.437
$\theta(\text{CO})$ (deg) <sup>a</sup>	3.3	0.9	2.6	4.1	0.6	1.44
$\nu(\text{C-O})$ (cm <sup>-1</sup> )	1979 (1970) <sup>b</sup>	1702	1724	1969 (1970) <sup>b</sup>	1666	1739
$\nu(\text{M-C})$ (cm <sup>-1</sup> )	510	356	358	482	355	351
bending modes (cm <sup>-1</sup> )	412 409	258 247	221 215	396 389	315 301	251 231
other modes (cm <sup>-1</sup> )	0 to 208	0 to 205	0 to 201	0 to 265	0 to 254	0 to 226

<sup>a</sup> $h(\text{C})$  denotes the distance from C to the first surface layer, and  $\theta(\text{CO})$  denotes the tilt angle of CO. <sup>b</sup>Ref. [39].

TABLE II: Adsorption energies, structural properties, and vibrational frequencies calculated using density-functional theory and density-functional perturbation theory for CO adsorbed on ruthenium-covered Pt(111) surfaces.

### III. RESULTS

We report the results of our density-functional calculations in Tables I and II. For platinum surfaces, the calculated atop binding energy  $E_{\text{ads}}(\text{atop}) = 1.61$  eV is consistent with that reported in Ref. [41] (1.55 eV in the same adsorption structure). As a matter of comparison, the experimental heat of adsorption at 1/4 ML CO is 1.30 eV. The relative adsorption energy  $E_{\text{ads}}(\text{atop}) - E_{\text{ads}}(\text{fcc})$  is calculated to be 0.13 eV, in accordance with the gradient-corrected relative adsorption energies (ranging from  $-0.10$  to  $-0.25$  eV) reported in Ref. [18]. As expected, our density-functional calculations favor CO adsorption at the threefold fcc and hcp adsorption sites for platinum and platinum-ruthenium surfaces, confirming the aforementioned disagreement with experiments. (Note that bridge adsorption of CO on platinum-ruthenium surfaces is predicted to be energetically unstable.) Despite this noteworthy failure, the bond length  $d(\text{C-O})$  is calculated to be  $1.153$  Å at the atop site and  $1.177$  Å at the bridge site on platinum, in good agreement with experimental bond lengths ( $1.15 \pm 0.05$  Å at both the atop and fcc sites). Similarly, the distance  $d(\text{Pt-C})$  from the carbon to its nearest platinum neighbor, calculated to be  $1.864$  Å at the atop site and  $2.029$  Å at the fcc site, is always within experimental error (experimental bond lengths are  $1.85 \pm 0.1$  Å and  $2.08 \pm 0.07$  Å at the atop and fcc sites, respectively). Note that both bond lengths increase with coordination.

The full phonon spectra for CO adsorbed at the atop, bridge, hcp, and fcc sites on platinum and platinum-ruthenium surfaces are calculated using density-functional perturbation theory (DFPT) [42]. Within this approach, the full dynamical matrix of the system is computed exactly by solving the self-consistent linear-response problem describing the electron response to atomic perturbations of arbitrary wavelength. The DFPT spectra reported in Tables I and II exhibit some common and expected features. The highest vibrational frequency in the range  $[1700 \text{ cm}^{-1}, 2100 \text{ cm}^{-1}]$  corresponds to the localized C-O stretching mode. The second highest frequency  $\nu(\text{M-C})$  in the range  $[300 \text{ cm}^{-1}, 600 \text{ cm}^{-1}]$  is related to the stretching of the metal-carbon bond. This mode is followed by two CO bending modes with frequencies lying  $20\text{-}200 \text{ cm}^{-1}$  below  $\nu(\text{M-C})$ . All the other modes involving displacements of the heavy metal atoms are found in the frequency range  $[0 \text{ cm}^{-1}, 300 \text{ cm}^{-1}]$ .

We now focus on the dependence of the C-O stretching frequency as a function of the adsorption site. Upon atop adsorption on platinum, the predicted  $\nu(\text{C-O})$  is reduced from  $2140 \text{ cm}^{-1}$  to  $2050 \text{ cm}^{-1}$ , corresponding to a red shift  $\Delta\nu(\text{C-O})$  of  $-90 \text{ cm}^{-1}$ . For comparison, the experimental stretching frequency, as obtained by means of sum-frequency generation (SFG) spectroscopy [39], decreases from  $2170 \text{ cm}^{-1}$  to  $2070 \text{ cm}^{-1}$ , corresponding to  $\Delta\nu(\text{C-O}) = -100 \text{ cm}^{-1}$ . The frequency shifts are even more marked at high-coordination sites:  $\nu(\text{C-O})$  is predicted to be  $1845 \text{ cm}^{-1}$ ,  $1752 \text{ cm}^{-1}$ , and  $1743 \text{ cm}^{-1}$  at the bridge, hcp, and fcc sites, corresponding to red shifts of up to  $-397 \text{ cm}^{-1}$ . These DFPT stretching frequencies show remarkable agreement with their SFG counterparts:  $\nu(\text{C-O}) = 1830 \text{ cm}^{-1}$  at the twofold bridge site,  $\nu(\text{C-O}) = 1760 \text{ cm}^{-1}$  at the threefold hcp and fcc sites, corresponding to a maximum red shift of  $-410 \text{ cm}^{-1}$ . Accurate DFPT frequencies are also obtained for CO adsorbed on platinum-ruthenium bimetallic surfaces. Indeed, the calculated stretching frequencies  $1979 \text{ cm}^{-1}$  (1 Ru ML) and  $1969 \text{ cm}^{-1}$  (2 Ru ML) at the atop site compare very closely to the SFG result of  $1970 \text{ cm}^{-1}$ .

In conclusion, all calculated CO stretching frequencies deviate by less than 2% from the measured ones, irrespective of the adsorption site and nature of the metal surface. The correct prediction of

	gas phase	atop	bridge	hcp	fcc
$f_{2\pi_x^*}/2 + f_{2\pi_y^*}/2$	0.00	0.25	0.37	0.41	0.41
$f_{5\sigma}$	1.00	0.92	0.92	0.92	0.92
$f_{1\pi_x}/2 + f_{1\pi_y}/2$	1.00	1.00	0.99	0.99	0.99
$f_{4\sigma^*}$	1.00	1.00	1.00	1.00	1.00
$f_{3\sigma}$	1.00	1.00	1.00	1.00	1.00
bond order	3.00	2.35	2.16	2.09	2.09

TABLE III: Molecular occupations and bond order for CO in the gas phase and for CO adsorbed on platinum.

the frequency red shifts allows the direct recognition of CO adsorption sites and confirms that CO preferentially occupies atop sites on platinum-ruthenium bimetallic surfaces. This very close agreement with experiment is made more remarkable by the lack of accuracy of the PBE-GGA adsorption energies. In the remainder of this work, we show how this accuracy can be rationalized in terms of the hybridization of the CO molecular orbitals with the metal bands.

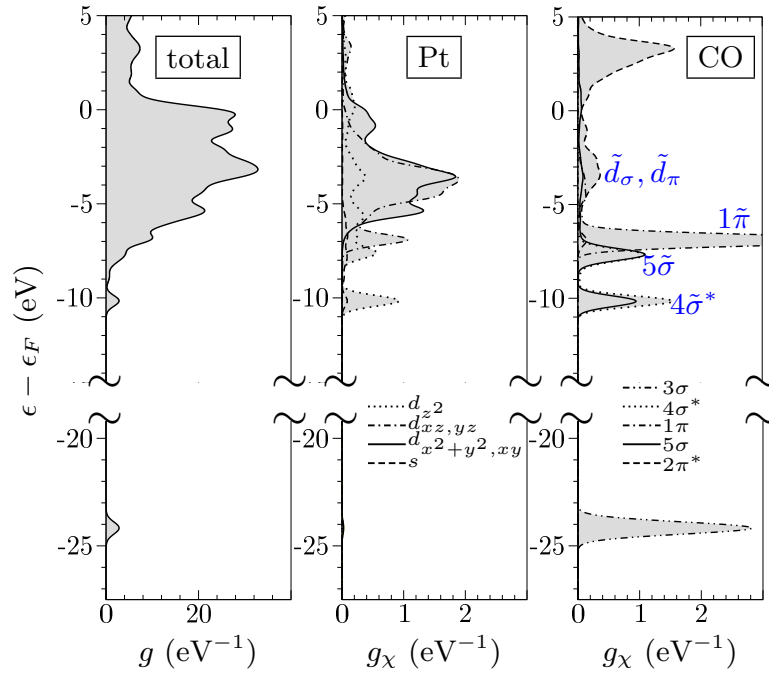
## IV. DISCUSSION

### A. Electronic Origins of the Frequency Shifts

The hybridization of the metal d bands with the  $2\pi^*$  lowest unoccupied molecular orbitals (LUMOs) and the  $5\sigma$  highest occupied molecular orbital (HOMO) plays a predominant role in the adsorption energy of CO on transition metals. According to the Blyholder model [43], these electronic interactions result in electron donation (i.e., partial depletion of the  $5\sigma$  orbital) and electron backdonation (i.e., partial filling of the  $2\pi^*$  orbital). It has been shown that the trends of the adsorption energies of CO on transition-metal surfaces can be correlated to the amounts of donation and backdonation (Hammer-Morikawa-Nørskov model) [12]. Among the suggested solutions to the “CO/Pt(111) puzzle”—e.g., nonequivalent GGA description of different bond orders [22], incorrect singlet-triplet CO excitation energies [23], effect of metal semicore polarization [24]—Kresse, Gil, and Sautet have proposed that the inaccuracy of density-functional calculations in determining the most stable adsorption site is due to an overestimation of the interaction between the  $2\pi^*$  orbitals and the metal bands, resulting from an underestimation of the HOMO-LUMO gap [21]. As discussed in the next section, this interpretation recovers the essential features of CO adsorption on transition metals: it identifies the tendency of local and generalized-gradient DFT to delocalize and overhybridize electronic states. Nevertheless, as shown below, the site-dependence of the C–O bond length and vibrational frequency is not affected by the LUMO and HOMO hybridizations. In other words, the hybridizations that subtly determine the relative CO adsorption energies do not influence the structural and vibrational predictions.

To establish this fact, we first introduce a spectral force analysis. The main objective of this analysis is to separate and assess the contribution from each CO molecular orbital to the force  $F$  acting on a given atom. The central quantity we introduce is  $\Phi_{I,\chi}(\epsilon)$ , the force density of states (FDOS) of the orbital  $\chi$ , which is defined as the  $\chi$ -resolved density of states weighted by the wavefunction contribution

(a) Atop DOS



(b) Fcc DOS

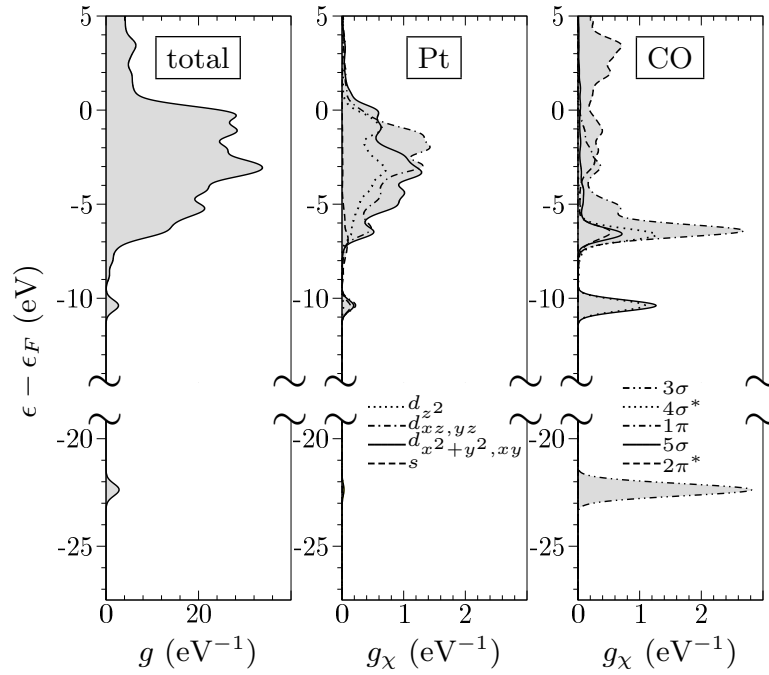
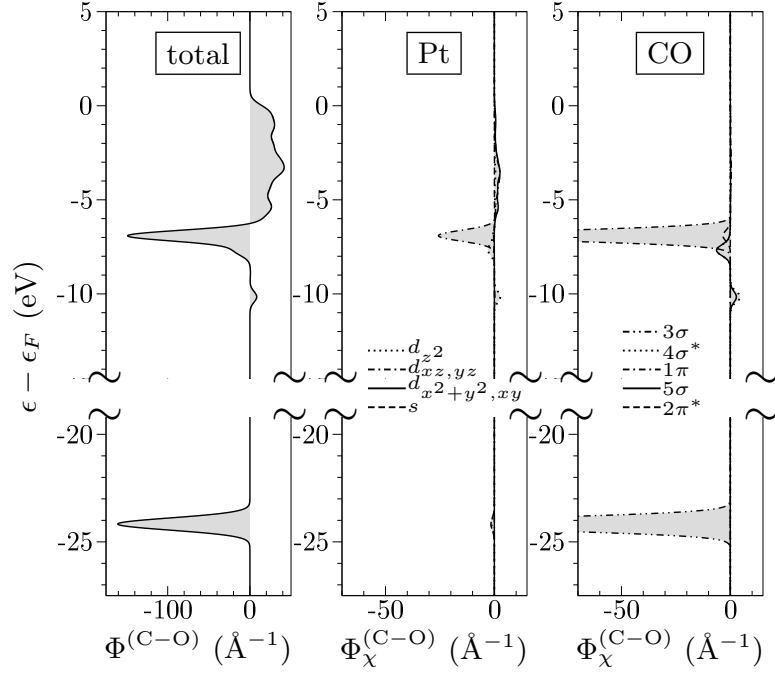


FIG. 1: Total density of states, density of states projected on the Pt atomic orbitals, and density of states projected on the CO molecular orbitals for atop and fcc adsorption of CO on Pt(111).

## (a) Atop FDOS



## (b) Fcc FDOS

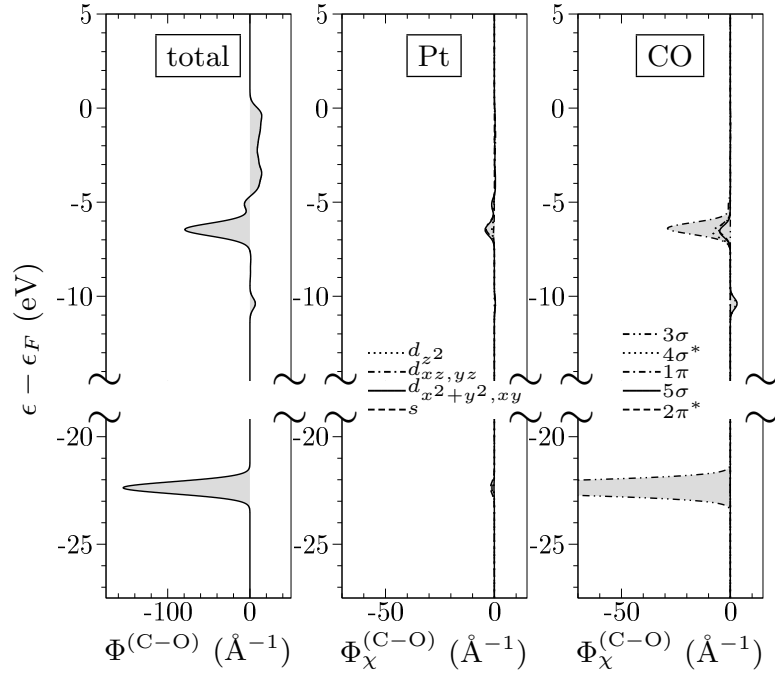


FIG. 2: Total force density of states, force density of states projected on the Pt atomic orbitals, and force density of states projected on the CO molecular orbitals for atop and fcc adsorption of CO on Pt(111).

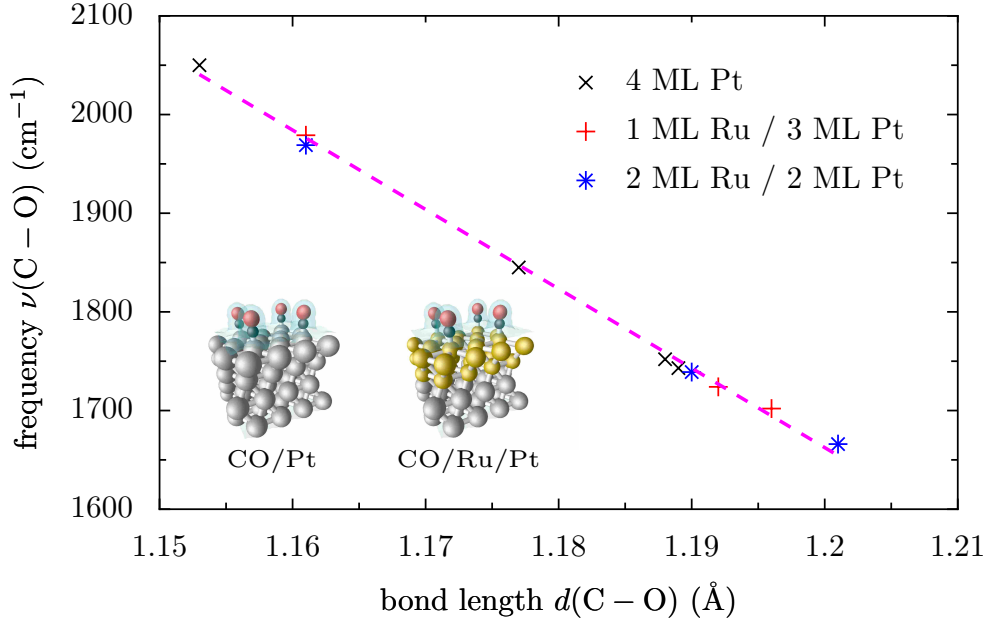


FIG. 3: Correlation between bond length and intramolecular frequency for CO on clean and ruthenium-covered Pt(111) surfaces.

to the force  $\mathbf{F}_I$  acting on atom  $I$ . To be more explicit, the FDOS of a given CO molecular orbital  $\chi$  can be expressed as:

$$\Phi_{I,\chi}(\epsilon) = \sum_i \mathbf{F}_{I,i} |\langle \chi | \psi_i \rangle|^2 \delta(\epsilon - \epsilon_i), \quad (1)$$

where  $\psi_i$  denotes the electronic wavefunction,  $\epsilon_i$  is the electronic energy, and  $\mathbf{F}_{I,i} = -f_i \int |\psi_i|^2 \partial v / \partial \mathbf{R}_I$  is the wavefunction contribution to the force  $\mathbf{F}_I$ . (The calculation of the overlap  $\langle \chi | \psi_i \rangle$  in the ultrasoft formalism is detailed in Appendix A.) It should be noted that, by summing the integrated FDOS  $\Phi_{I,\chi}(\epsilon)$  over a complete set of orbitals satisfying orthonormality, one obtains the total electronic force acting on atom  $I$ . As a consequence, the FDOS can be quantitatively connected to relevant observables. Additionally, by projecting the force density of states along the normalized atomic displacements  $\Delta_I^{\text{C-O}}$  corresponding to the C–O stretching mode, we obtain the force density of states along the stretching mode  $\Phi_\chi^{\text{C-O}}(\epsilon) = \sum_I \Delta_I^{\text{C-O}} \cdot \Phi_{I,\chi}(\epsilon)$ , to be heuristically identified as the orbital contribution to the intramolecular force.

The orbital-projected density of states (DOS)  $g_\chi(\epsilon) = \sum_i |\langle \chi | \psi_i \rangle|^2 \delta(\epsilon - \epsilon_i)$  is commonly used to provide an insightful picture of the electronic hybridizations that take place when CO is adsorbed on platinum. Similarly,  $\Phi_\chi^{\text{C-O}}(\epsilon)$  describes the influence of electronic hybridizations on the force along the C–O stretching mode. The projected densities of states  $g_\chi(\epsilon)$  and projected force densities of states  $\Phi_\chi^{\text{C-O}}(\epsilon)$  for different adsorption sites are plotted in Figures 1 and 2. A detailed analysis of the orbital-resolved densities of states is given in Ref. [21]. For the purpose of our study, we emphasize the following features. When CO adsorbs on Pt(111), the  $4\sigma^*$  and  $5\sigma$  orbitals hybridize with the metal  $d_{z^2}$



band, generating  $4\tilde{\sigma}^*$  and  $5\tilde{\sigma}$  states with mainly adsorbate character (adopting the terminology of Ref. [44], the tilde symbol denotes hybrid states). These  $4\tilde{\sigma}^*$  and  $5\tilde{\sigma}$  states are found in the energy ranges  $[-12 \text{ eV}, -9 \text{ eV}]$  and  $[-9 \text{ eV}, -5 \text{ eV}]$  relative to the Fermi level. Above  $-5 \text{ eV}$ , the  $5\sigma$  orbital and the  $d_{z^2}$  band generate a  $\tilde{d}_\sigma$  band with predominant metal character. This interaction results in a partial depletion of the  $5\sigma$  HOMO (electron donation). In addition, the interaction between the  $1\pi$  and  $2\pi^*$  orbitals and the  $d_{xz}$  and  $d_{yz}$  bands produces  $1\tilde{\pi}$  states in the range  $[-9 \text{ eV}, -5 \text{ eV}]$  and a broad  $\tilde{d}_\pi$  band above  $-5 \text{ eV}$ , causing partial occupation of the  $2\pi^*$  LUMOs (electron backdonation) [43]. The changes in molecular orbital occupations due to CO adsorption are reported in Table III.

In order to understand how the generation of these hybrid states affects the intramolecular force, we turn to the FDOS (Figure 2). The graphs are plotted according to the convention that bonding states (i.e., opposed to the stretching of the C–O bond) correspond to negative values of  $\Phi_\chi^{\text{C-O}}$ . First, we note that the bonding contribution from the  $3\sigma$  state does not vary with the adsorption site, confirming that the  $3\sigma$  state retains a strong molecular character. Additionally, we observe that the  $5\tilde{\sigma}$  and  $1\tilde{\pi}$  states are bonding while the  $4\tilde{\sigma}^*$  is antibonding, as expected intuitively. In the energy region above  $-5 \text{ eV}$ , another contribution appears. This contribution corresponds to high-energy wavefunctions located inside the platinum slab, as evidenced by the absence of any molecular-orbital force contribution above  $-5 \text{ eV}$ . Nevertheless, due to their metal character, the contribution of these high-energy wavefunctions is mostly canceled by the positively charged platinum cores. Consequently, the local contribution from the hybrid states of strong molecular character prevails.

Besides these observations, the main feature of the FDOS graphs is the predominant bonding contribution between  $-9 \text{ eV}$  and  $-5 \text{ eV}$ . At the atop site, the curve displays a sharp negative peak which corresponds mainly to the  $1\pi$  orbital-resolved contribution  $\Phi_{1\pi}^{\text{C-O}}(\epsilon)$ . At the fcc site, both the magnitude and the relative share of the peak are reduced, clearly indicating that the  $1\tilde{\pi}$  states have more influence on the change in intramolecular bonding than any of the other hybrid wavefunctions. The  $1\tilde{\pi}$  states maintain a predominant  $1\pi$  character at the atop site, whereas at high-coordination sites this molecular character is significantly reduced due to a stronger hybridization with the substrate. Therefore, the  $1\pi$  bonding contribution to the intramolecular force decreases with site coordination. As intramolecular bonding decreases, the C–O bond length increases. The predominance of the  $1\pi$  bonding contribution is confirmed by the density-distribution analysis initially introduced by Zupan, Burke, Ernzerhof, and Perdew [45], as discussed in Appendix B.

For CO adsorbed on transition metal surfaces, the intramolecular bond length and the intramolecular stretching frequency are strongly correlated. An extensive study of Gajdoš, Eichler, and Hafner [46] showed a linear correlation between  $d(\text{C-O})$  and  $\nu(\text{C-O})$  for CO adsorbed on close-packed transition metals:  $\nu(\text{C-O})$  shifts down in frequency as  $d(\text{C-O})$  increases. As illustrated in Figure 3, a similar trend is observed for CO adsorbed on ruthenium-covered platinum surfaces. Therefore, the increase in C–O bond length at high-coordination sites, which reflects a decrease in  $1\pi$  bonding contribution, is accompanied by a reduction of the C–O stretching frequency.

While the preceding is consistent with the interpretation given in Refs [43, 44, 46], it is important to make one central observation: although the LUMO  $2\pi^*$  filling is a reasonable measure of the amount of hybridization between the  $1\pi$ ,  $2\pi^*$  orbitals and the metal  $d_{xz}$ ,  $d_{yz}$  bands, filling the  $2\pi^*$  orbitals does not directly weaken the bond, as evidenced by the very low values of  $\Phi_{2\pi^*}^{(\text{C-O})}$  in the energy range  $[-9$

eV,  $-5$  eV]. This interpretation helps explain the fact that the CO adsorption energies do not show a well-defined relationship with the C–O stretching frequency [47, 48].

The main conclusion of this section is as follows. At variance with the CO adsorption energies, electron backdonation and electron donation have little direct bearing on the intramolecular forces. Their immediate effect on the molecular bond length and stretching frequency cannot account for the observed shifts. Instead, the changes in bond length and stretching frequency are primarily related to the hybridization of the  $1\pi$  molecular orbitals. This provides important indications as to why the structural and vibrational properties of CO adsorbed on platinum and platinum-ruthenium surfaces are accurately predicted. The GGA + molecular U study presented in the next part provides additional quantitative evidence in support to this conclusion.

### B. Influence of Donation and Backdonation on the Accuracy of the Frequency Predictions

As mentioned above, the failure of density-functional calculations in predicting CO adsorption energies is traceable to an overhybridization of the CO molecular orbitals with the metal bands [21, 49]. To assess the influence of this overhybridization on the accuracy of the calculated adsorption energies, bond lengths, and vibrational properties, we have performed a sensitivity analysis. This analysis consists of controlling and varying the HOMO and LUMO hybridizations, while monitoring the variations of the mentioned observables. To this end, we have used the GGA + molecular U approach introduced by Kresse, Gil, and Sautet [21]. This approach (inspired by the LDA + U method [50]) consists of adding an orbital-dependent term to the GGA energy functional, thus imposing a penalty on orbital hybridization.

We employ the following GGA + molecular U energy functional:

$$E_{GGA+U} = E_{GGA} + \frac{U_{2\pi^*}}{2} \sum_{\sigma} \text{Tr}\{\mathbf{f}_{2\pi^*,\sigma}(\mathbf{I} - \mathbf{f}_{2\pi^*,\sigma})\} + \frac{U_{5\sigma}}{2} \sum_{\sigma} f_{5\sigma,\sigma}(1 - f_{5\sigma,\sigma}),$$

where  $f_{5\sigma,\sigma}$  is the occupation of the  $5\sigma$  orbital of spin  $\sigma$  and  $\mathbf{f}_{2\pi^*,\sigma}$  is the occupation matrix associated with the  $2\pi_x^*$  and  $2\pi_y^*$  orbitals of spin  $\sigma$ . The parameters  $U_{2\pi^*}$  and  $U_{5\sigma}$  penalize noninteger occupations of the  $2\pi^*$  and  $5\sigma$  orbitals:  $U_{2\pi^*}$  reduces  $2\pi^*$  backdonation while  $U_{5\sigma}$  reduces  $5\sigma$  donation, as illustrated in Figure 4. The parameters  $U_{2\pi^*}$  and  $U_{5\sigma}$  can also be interpreted as shifting the effective single-electron energies. Heuristically,  $U_{\chi}$  modifies the single-electron energy  $\epsilon_{\chi}$  by an amount  $U_{\chi}(1/2 - f_{\chi})$ . Thus,  $U_{2\pi^*}$  increases the  $2\pi^*$  energies, whereas  $U_{5\sigma}$  decreases the  $5\sigma$  energy, causing the HOMO-LUMO gap to increase.

The present functional differs slightly from that introduced by Kresse, Gil, and Sautet. The GGA + molecular U energy in Eq. 2, whose expression is based on the matrix formulation introduced by Cococcioni and de Gironcoli [51], is invariant with respect to the choice of the  $x$ - and  $y$ -axes. In other words, an arbitrary rotation of the molecular orbitals does not affect the GGA + molecular U energy. Additionally, the functional allows the freedom to vary both the amount of electron backdonation and that of electron donation. The necessity of simultaneously varying backdonation and donation will be discussed later.

Although a molecular U term is admittedly a simplified energy correction, it reproduces the essential

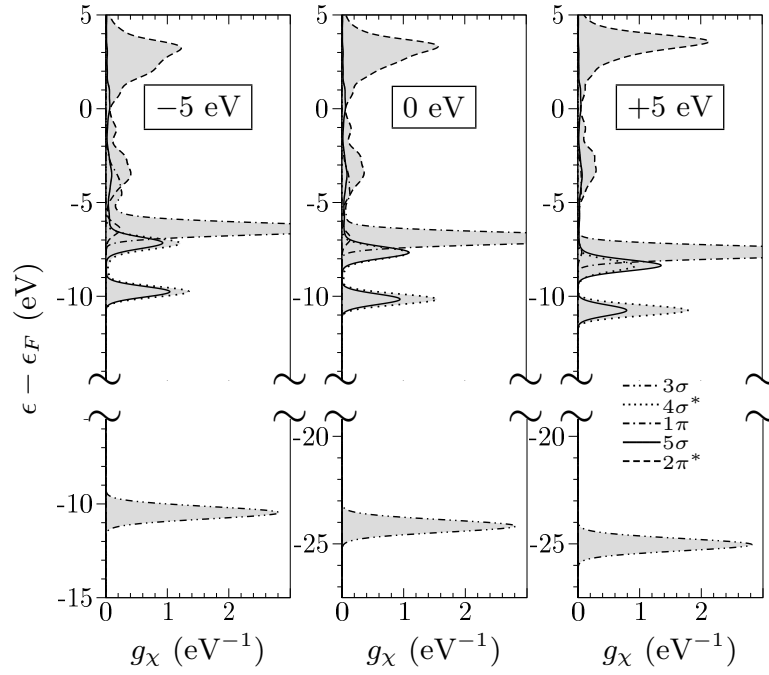
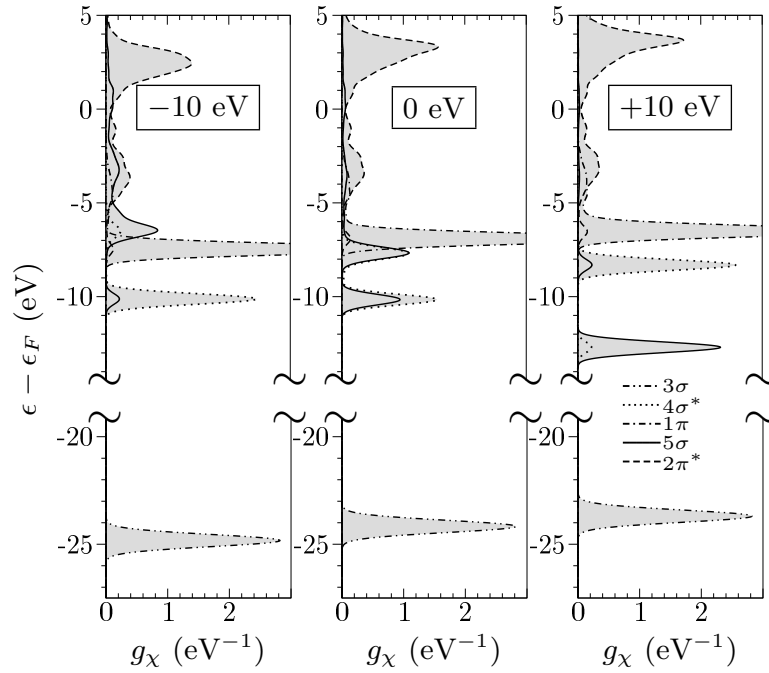
(a) Atop DOS vs.  $U_{2\pi^*}$ (b) Atop DOS vs.  $U_{5\sigma}$ 

FIG. 4: Density of states projected on the CO molecular orbitals as a function of  $U_{2\pi^*}$  and  $U_{5\sigma}$  controlling the hybridization of the LUMO and HOMO orbitals for atop adsorption of CO on Pt(111).

features of the energetics of CO adsorption [21]. The cluster calculations of Gil *et al.*, based on the B3LYP hybrid functional [52], confirm that the inaccuracy of the GGA energies can be ascribed to an overhybridization of the  $2\pi^*$  molecular orbitals [49]. This conclusion is supported by the recent periodic-slab B3LYP calculations of Neef and Doll [25, 26]. Moreover, experimental studies indicate that the adsorption energy of CO on platinum shows a linear dependence with respect to the energy of the center of the metal d bands, in agreement with the theoretical model developed by Hammer, Morikawa and Nørskov [12]. However, the coefficient of proportionality is overestimated within density-functional calculations, indicating that the interaction between the  $2\pi^*$  orbitals and the metal d bands is excessive.

We thus proceeded to calculate the energetic, structural, and vibrational properties for CO adsorbed on platinum. Stretching frequencies are now obtained by diagonalizing the two-by-two dynamical matrix associated off-equilibrium displacements of the carbon and oxygen atoms in the direction normal to the surface. Due to the large atomic mass of platinum, the resulting stretching frequencies deviate by less than  $1 \text{ cm}^{-1}$  from the full DFPT phonon frequencies.

The results of the calculations are presented in Figure 5, and in Appendix C, along with methodological details. As expected, adsorption energies decrease with increasing penalization on the hybridizations of the HOMO and LUMOs. Consequently, both donation and backdonation favor CO adsorption, in agreement with Ref. [21]. Moreover, we observe that electron backdonation tends to decrease the relative adsorption energy  $E_{\text{ads}}(\text{atop}) - E_{\text{ads}}(\text{fcc})$ , confirming that  $2\pi^*$  backdonation favors CO adsorption at high-coordination sites, as demonstrated by Anderson and Awad [53]. Additionally, the effect of  $U_{5\sigma}$  on the relative binding energy is much weaker than that of  $U_{2\pi^*}$ . This result supports the hypothesis that the failure of density-functional calculations in predicting the most stable adsorption site is principally related to an overestimation of  $2\pi^*$  backdonation [19, 20, 21].

Considering now the structural and vibrational properties, we observe more complex  $U_{2\pi^*}$ - and  $U_{5\sigma}$ -dependencies. The effect of electron donation must clearly be taken into account when analyzing the sensitivity of the calculated stretching frequencies. Note that the invariance of the stretching frequency with respect to  $U_{2\pi^*}$  for CO adsorbed at the atop site, as already observed in Ref. [19] for copper surfaces, can be explained by the fact that the  $U_{2\pi^*}$ -axis is tangent to the contour line  $\nu(\text{C-O}) = 2050 \text{ cm}^{-1}$ . Despite this fact, the dependence of  $\nu(\text{C-O})(\text{atop})$  with respect to  $U_{5\sigma}$  is appreciable, supporting the idea that  $2\pi^*$  backdonation alone does not control the site-dependence of the C-O stretching frequency.

To conclude this section, we report the results of our sensitivity analysis (Figure 6). Large ranges for  $U_{2\pi^*}$  and  $U_{5\sigma}$  are selected:  $0 \text{ eV} < U_{2\pi^*} < 5 \text{ eV}$  and  $-10 \text{ eV} < U_{5\sigma} < 10 \text{ eV}$ . Note that the parameter  $U_{2\pi^*}$  is kept positive since the GGA + molecular U calculations clearly indicate that  $2\pi^*$  backdonation is overestimated. We emphasize that these energy ranges correspond to large shifts in the single-electron energies (up to  $\Delta\epsilon_{2\pi^*} = 1 \text{ eV}$  and  $|\Delta\epsilon_{5\sigma}| = 4 \text{ eV}$ ) and to large variations of the adsorption energies (up to  $|\Delta E_{\text{ads}}| = 1.5 \text{ eV}$ ). Thus, the relative variations of the adsorption energies are comparable to their absolute values. Despite these sizable variations of the adsorption energies, we observe little variations

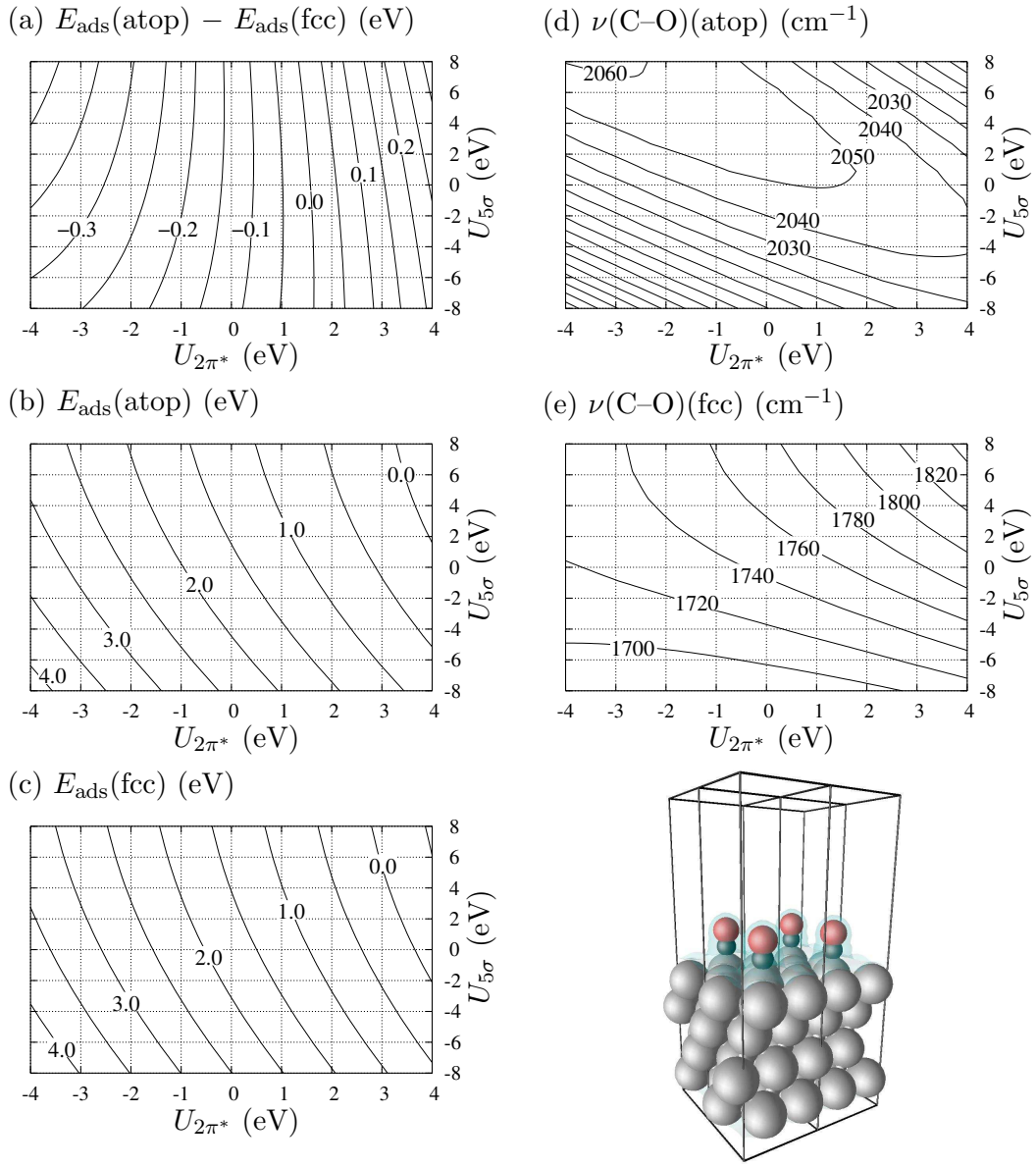
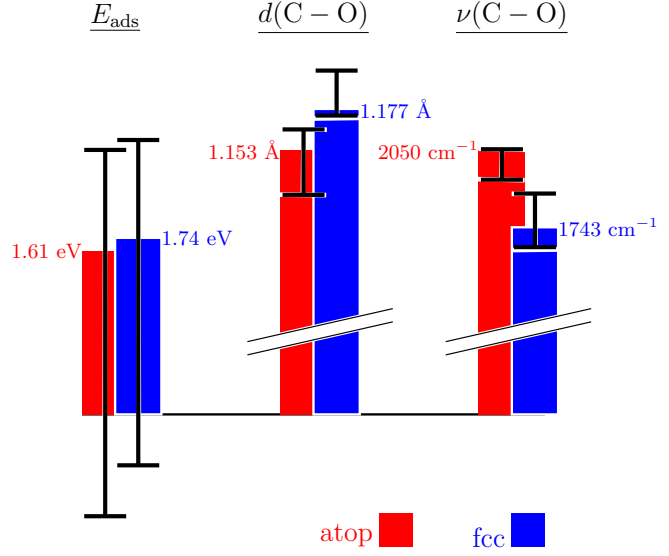


FIG. 5: Adsorption energy and intramolecular stretching frequency as a function of  $U_{2\pi^*}$  and  $U_{5\sigma}$  controlling the hybridization of the LUMO and HOMO orbitals for atop and fcc adsorption of CO on Pt(111).

FIG. 6: Ranges of variation (indicated by black error bars) of the adsorption energy, bond length, and stretching frequency of CO on Pt(111) for a very broad range of hybridizations ( $0 \text{ eV} < U_{2\pi^*} < 5 \text{ eV}$  and  $-10 \text{ eV} < U_{5\sigma} < 10 \text{ eV}$ ).



of the bond lengths and stretching frequencies:

$$\begin{cases} 1.127 \text{ Å} < d(\text{C}-\text{O})(\text{atop}) < 1.165 \text{ Å} \\ 1.173 \text{ Å} < d(\text{C}-\text{O})(\text{fcc}) < 1.199 \text{ Å} \\ 1933 \text{ cm}^{-1} < \nu(\text{C}-\text{O})(\text{atop}) < 2055 \text{ cm}^{-1} \\ 1666 \text{ cm}^{-1} < \nu(\text{C}-\text{O})(\text{fcc}) < 1878 \text{ cm}^{-1} \end{cases} \quad (2)$$

These small variations account for the remarkable accuracy of the bond lengths and stretching frequencies calculated within PBE-GGA. In particular, they justify the correct ordering of the C–O stretching frequencies despite important qualitative errors in predicting the relative CO adsorption energies. These results provide strong support to the conclusion of the preceding section: the variations of  $d(\text{C}-\text{O})$  and  $\nu(\text{C}-\text{O})$  are not directly due to electron donation and backdonation, but rather to the hybridization of the  $1\pi$  orbitals.

## V. CONCLUSION

This study has evidenced that the PBE-GGA predictions for the stretching frequencies of CO adsorbed on platinum are in excellent agreement with SFG experiments despite the well-known failure of local and generalized-gradient calculations in predicting the most stable adsorption site. Similar agreement is obtained for CO adsorbed on platinum-ruthenium bimetallic surfaces, allowing the direct recognition of CO adsorption sites.

Our orbital-resolved force analysis has demonstrated that the variations of bond length and stretching frequency as a function of the CO adsorption site are principally due to the  $1\pi$  hybridization, rather than the  $2\pi^*$  and  $5\sigma$  hybridizations. Using the GGA + molecular U approach, we have performed a

sensitivity analysis to quantify the influence of the  $2\pi^*$  and  $5\sigma$  hybridizations on the structural and vibrational properties for CO on platinum. The effect of  $2\pi^*$  backdonation has been shown to be small and comparable to that of  $5\sigma$  donation, contradicting the widespread idea that backdonation controls the frequency shifts.

These results explain the remarkable accuracy of the PBE-GGA frequency predictions despite errors in the hybridizations of the  $2\pi^*$  and  $5\sigma$  orbitals. Furthermore, they suggest a promising way to connect density-functional calculations with experiments in some of the most problematic cases of molecular adsorption on transition metals.

### Acknowledgments

The calculations in this work have been performed using the Quantum-Espresso package (GNU General Public License). The authors acknowledge support from the MURI grant DAAD 19-03-1-0169. I. D. personally thanks the École Nationale des Ponts et Chaussées (France) and the Martin Family Society of Fellows for Sustainability for their help and support. Valuable discussions with Matteo Cococcioni, Cody Friesen, and Fabien Sorin are gratefully acknowledged.

### APPENDIX A: ULTRASOFT OVERLAPS

The Vanderbilt ultrasoft formalism [33] consists of replacing the density operator  $\hat{n}(\mathbf{r})$  with:

$$\hat{n}^{US}(\mathbf{r}) = \hat{n}(\mathbf{r}) + \sum_I \hat{n}_I(\mathbf{r}) \quad (\text{A1})$$

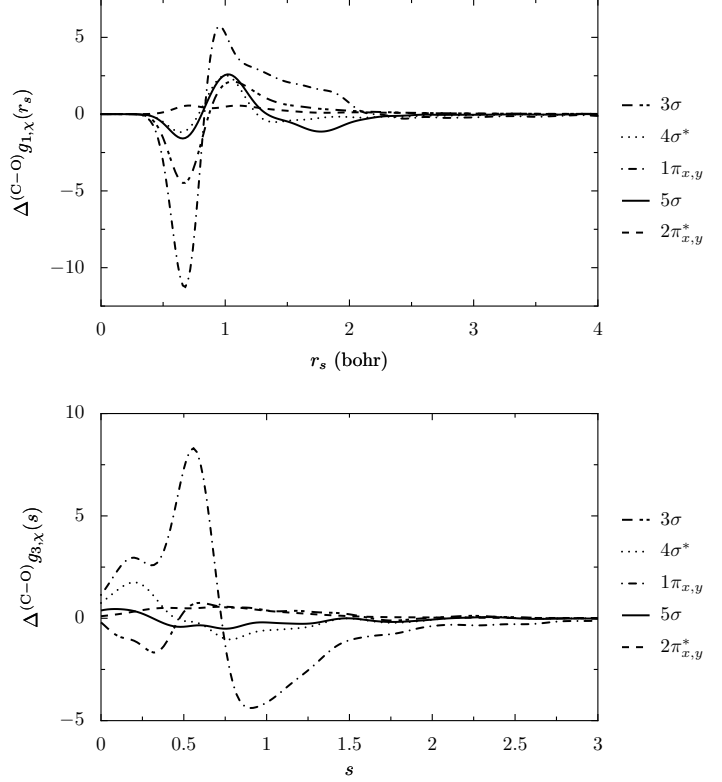
where  $\hat{n}_I(\mathbf{r}; \mathbf{r}_1, \mathbf{r}_2) = \sum_{n,m} Q_{I,n,m}(\mathbf{r}) \beta_{I,n}^*(\mathbf{r}_1) \beta_{I,m}(\mathbf{r}_2)$  is the charge-augmentation contribution from the ionic core  $I$ . Correspondingly, the overlap operator  $\hat{S}$  becomes:

$$\hat{S} = \hat{1} + \sum_I \hat{S}_I \quad (\text{A2})$$

where  $\hat{S}_I(\mathbf{r}_1, \mathbf{r}_2) = \sum_{n,m} \int Q_{I,n,m}(\mathbf{r}) d\mathbf{r} \beta_{I,n}^*(\mathbf{r}_1) \beta_{I,m}(\mathbf{r}_2)$  is the ionic contribution to the overlap operator. The ultrasoft pseudopotential of the ionic core  $I$  is the sum of a local part  $v_I^L(\mathbf{r})$  and a nonlocal part  $\hat{v}_I^{NL}(\mathbf{r}_1, \mathbf{r}_2) = \sum_{n,m} D_{I,n,m}^0 \beta_{I,n}^*(\mathbf{r}_1) \beta_{I,m}(\mathbf{r}_2)$ .

This ultrasoft formalism considerably improves the convergence of density-functional algorithms with respect to the energy cutoffs applied to the plane-wave expansions of the wavefunctions and charge density. However, to calculate the overlap  $\langle \chi | \hat{S} | \psi \rangle$  between the molecular orbital  $\chi$  and the wavefunction  $\psi$ , it must be borne in mind that the overlap operators  $\hat{S}_\chi$  and  $\hat{S}_\psi$  corresponding to  $\chi$  and  $\psi$  are distinct since the molecular orbital is calculated without the platinum slab. The procedure employed here consists in including fictitious platinum cores in the calculation of the molecular orbital. These fictitious cores are obtained by setting the local and nonlocal part of the platinum pseudopotential to zero, while keeping the contribution to the overlap operator unchanged. The resulting operator  $\hat{S}_\chi^{fict}$  being identical to  $\hat{S}_\psi$ , the overlap coefficient can be calculated as  $\langle \chi^{fict} | \hat{S}_\chi^{fict} | \psi \rangle = \langle \chi^{fict} | \hat{S}_\psi | \psi \rangle$  where  $\chi^{fict}$  is the molecular orbital calculated in the presence of the fictitious platinum cores. The primary advantage of this procedure is that it only requires changing the pseudopotentials.

FIG. 7: Derivative of the density distribution function  $\Delta^{(\text{C-O})}g_{1,\chi}(r_s)$  and derivative of the density-gradient distribution function  $\Delta^{(\text{C-O})}g_{3,\chi}(s)$  along the C–O stretching mode for each molecular orbital  $\chi$ .



## APPENDIX B: DENSITY-DISTRIBUTION ANALYSIS

As an additional confirmation to the predominance of the  $1\pi$  contribution in the C–O intramolecular force, we have calculated the density distribution and density-gradient distribution [45] projected on each CO molecular orbital  $\chi$ . We define the projected density distribution as:

$$g_{1,\chi}(r_s) = \sum_i f_i |\langle \chi | \psi_i \rangle|^2 \int |\psi_i(\mathbf{r})|^2 \delta(r_s - r_s(\mathbf{r})) d\mathbf{r}, \quad (\text{B1})$$

where  $r_s$  is the Seitz radius. We propose a similar definition for the projected density-gradient distribution:

$$g_{3,\chi}(s) = \sum_i f_i |\langle \chi | \psi_i \rangle|^2 \int |\psi_i(\mathbf{r})|^2 \delta(s - s(\mathbf{r})) d\mathbf{r}, \quad (\text{B2})$$

where  $s = |\nabla n|/2k_F n$  is the reduced density gradient. The derivatives of the distribution functions along the C–O stretching mode  $\Delta^{(\text{C-O})}g_{n,\chi} = d(\text{C-O})\partial g_{n,\chi}/\partial d(\text{C-O})$  ( $n=1,3$ ) are plotted in Figure 7.

Considering  $\Delta^{(\text{C-O})}g_{1,\chi}(r_s)$ , we observe that increasing  $d(\text{C-O})$  tends to decrease the electronic charge in spatial regions of high electronic density. This trend is particularly marked for the  $1\pi$  molecular orbitals, confirming their predominance in the intramolecular force. The predominant  $1\pi$  contribution can also be seen in the  $\Delta^{(\text{C-O})}g_{3,\chi}(s)$  graph. It is important to note that the  $1\pi$  orbitals result in a significant increase in charge-density homogeneity. According to the bond-expansion criterion derived by Zupan, Burke, Ernzerhof, and Perdew (Eq. 9 in Ref [45]), this observation confirms that the  $1\pi$  orbitals are strongly bonding.



## APPENDIX C: GGA + MOLECULAR U FORCE DENSITY OF STATES

The calculation of the FDOS within GGA + molecular U can be performed along the same general lines as the method presented in Sec. IV A. the only modification being in the expression of the wavefunction contribution to the force  $\mathbf{F}_{I,i\sigma}$ . In the ultrasoft formalism and in the absence of molecular U contribution, the wavefunction contribution to the force can be written as [54, 55]:

$$(\mathbf{F}_{I,i\sigma})_{GGA} = -f_{i\sigma} \langle \psi_{i\sigma} | \frac{\partial \hat{v}}{\partial \mathbf{R}_I} - \epsilon_{i\sigma} \frac{\partial \hat{S}}{\partial \mathbf{R}_I} | \psi_{i\sigma} \rangle. \quad (C1)$$

Adding the molecular U term, the force contribution becomes:

$$\begin{aligned} (\mathbf{F}_{I,i\sigma})_{GGA+U} = (\mathbf{F}_{I,i\sigma})_{GGA} - \frac{U_{2\pi^*}}{2} \sum_{\sigma} \text{Tr} \left\{ (\mathbf{I} - 2\mathbf{f}_{2\pi^*,\sigma}) \frac{\partial \mathbf{f}_{2\pi^*,i\sigma}}{\partial \mathbf{R}_I} \right\} \bigg|_{\psi_{i\sigma}} \\ - \frac{U_{5\sigma}}{2} \sum_{\sigma} (1 - 2f_{5\sigma,\sigma}) \frac{\partial f_{5\sigma,i\sigma}}{\partial \mathbf{R}_I} \bigg|_{\psi_{i\sigma}} \end{aligned} \quad (C2)$$

where  $\mathbf{f}_{2\pi^*,i\sigma} = [f_{i\sigma} \langle \psi_{i\sigma} | \hat{S} | 2\pi^*_{\alpha} \rangle \langle 2\pi^*_{\beta} | \hat{S} | \psi_{i\sigma} \rangle]_{\alpha\beta}$  denotes the contribution from the wavefunction  $\psi_{i\sigma}$  to the  $2\pi^*$  occupation matrix  $\mathbf{f}_{2\pi^*,\sigma}$  and  $f_{5\sigma,i\sigma} = f_{i\sigma} \langle \psi_{i\sigma} | \hat{S} | 5\sigma \rangle \langle 5\sigma | \hat{S} | \psi_{i\sigma} \rangle$  is the contribution from  $\psi_{i\sigma}$  to  $f_{5\sigma,\sigma}$ . Note that the derivatives must be calculated keeping  $\psi_{i\sigma}$  fixed.

The main computational difficulty in determining the derivatives of the occupation coefficients is the evaluation of the response of the molecular orbitals  $\chi$  to the atomic displacements  $\partial \chi / \partial \mathbf{R}_I$ . These responses can be obtained by performing a separate calculation for an isolated CO molecule using the same linear-response approach as that employed in the phonon calculation [42]. The projected and total FDOS spectra as a function of the hybridization parameters for CO adsorbed at the atop site on Pt(111) are reported in Figures 8 and 9. The observed trends confirm that large shifts in the LUMO and HOMO single-electron energies do not affect the predominance of the  $1\pi$  contribution. For positive values of  $U_{2\pi^*}$  and  $U_{5\sigma}$ , the magnitude of the peak in the  $1\pi$  FDOS increases due to the stronger molecular character of the  $1\pi$  orbitals. Note that this increase in the  $1\pi$  bonding contribution is accompanied by an increase in the antibonding contribution from the metal bands. Similar compensation effects in the electronic forces can be observed for negative values of the hybridization parameters. In particular, for  $U_{2\pi^*}$  equal to  $-5$  eV corresponding to an unphysical overestimation of the  $2\pi^*$  hybridization the decrease in the bonding contribution from the  $1\pi$  orbitals is partially offset by the decrease in the antibonding contribution from the d bands. This observation provides a more specific understanding of the invariance of the stretching frequency as a function of the HOMO and LUMO hybridizations.

- 
- [1] J. E. Tester, E. M. Drake, M. J. Driscoll, M. W. Golay, and W. A. Peters, *Sustainable Energy* (MIT Press, 2005).
  - [2] J. Larminie and A. Dicks, *Fuel Cell Systems Explained* (Wiley-VCH, 2003), 2nd ed.
  - [3] W. Vielstich, A. Lamm, and H. Gasteiger, *Handbook of Fuel Cells: Fundamentals, Technology, Applications* (Wiley-VCH, 2003).
  - [4] N. P. Brandon and D. Thompsett, *Fuel Cells Compendium* (Elsevier, 2005).

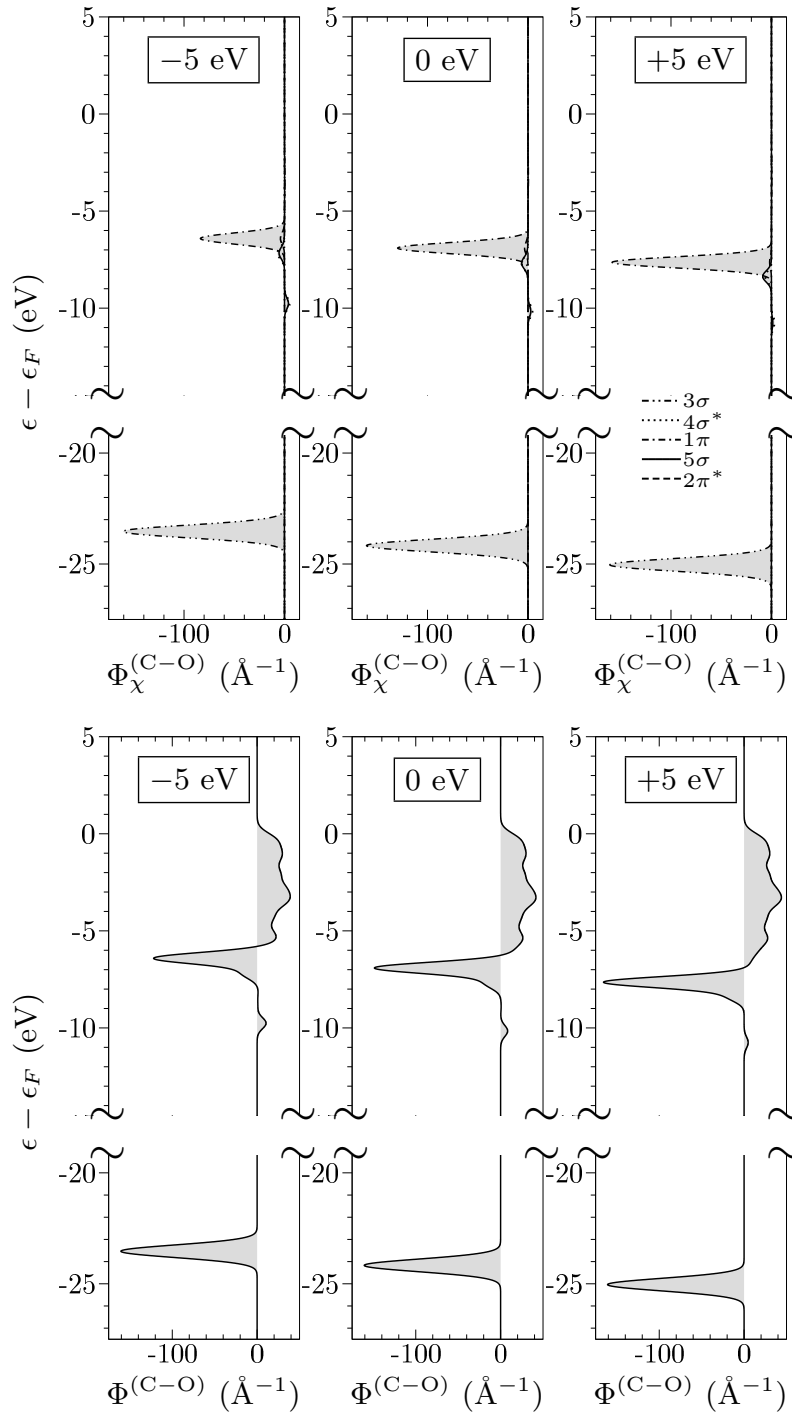
Atop FDOS vs.  $U_{2\pi^*}$ 

FIG. 8: Force density of states projected on the CO molecular orbitals, and total force density of states as functions of  $U_{2\pi^*}$  controlling the hybridization of the LUMO orbitals for atop adsorption of CO on Pt(111).

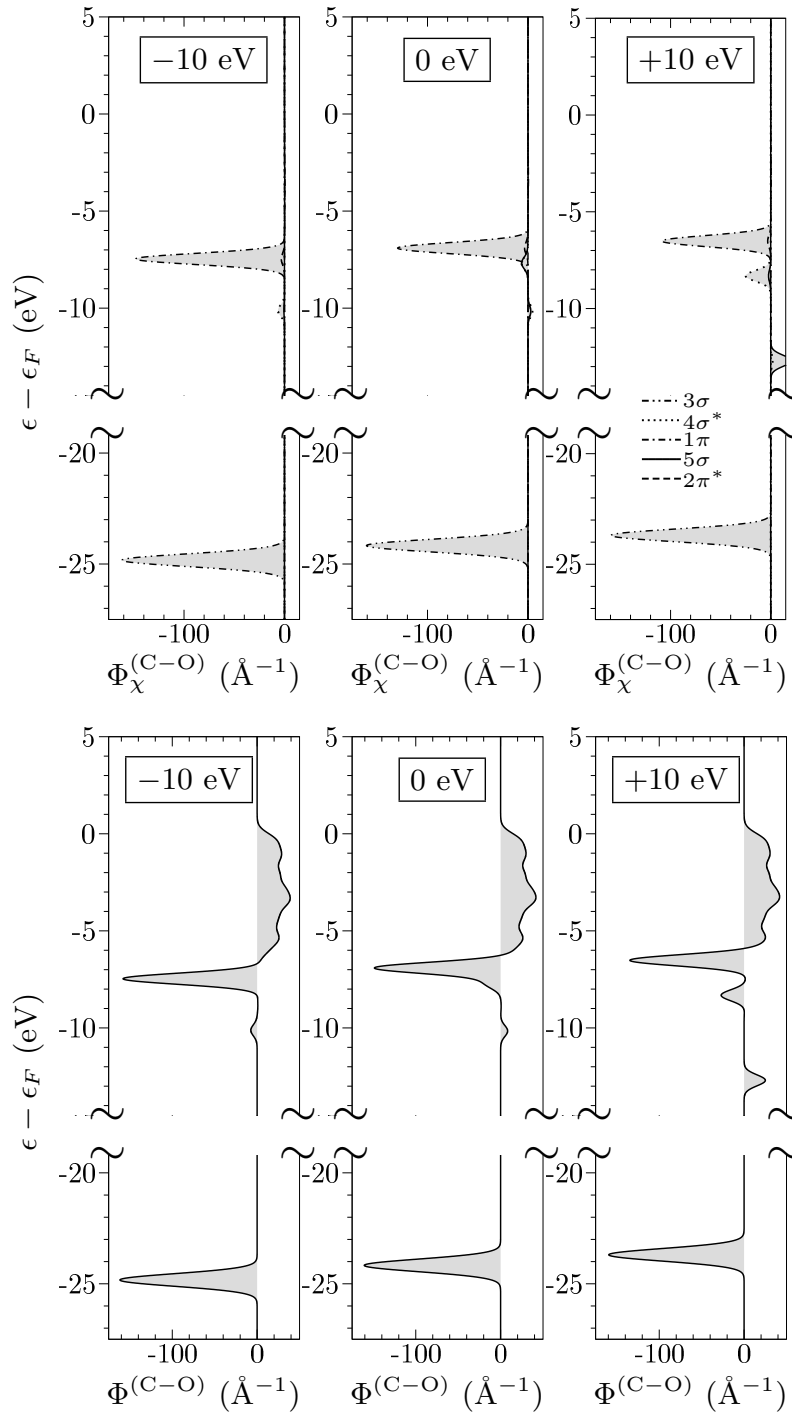
Atop FDOS vs.  $U_{5\sigma}$ 

FIG. 9: Force density of states projected on the CO molecular orbitals, and total force density of states as functions of  $U_{5\sigma}$  controlling the hybridization of the LUMO orbitals for atop adsorption of CO on Pt(111).

- [5] G. Hoogers, *Fuel Cell Technology Handbook* (CRC Press, 2003).
- [6] S. Cramm, K. A. Friedrich, K. P. Geyzers, U. Stimming, and R. Vogel, *Fres. J. Anal. Chem.* **358**, 189 (1997).
- [7] E. Herrero, J. M. Feliu, and A. Wieckowski, *Langmuir* **15**, 4944 (1999).
- [8] A. Crown, C. Johnston, and A. Wieckowski, *Surf. Sci.* **506**, L268 (2002).
- [9] Y. Y. Tong, H. S. Kim, P. K. Babu, P. Waszczuk, A. Wieckowski, and E. Oldfield, *J. Am. Chem. Soc.* **124**, 468 (2002).
- [10] F. Maillard, G. Q. Lu, A. Wieckowski, and U. Stimming, *J. Phys. Chem. B* **109**, 16230 (2005).
- [11] P. Liu, A. Logadottir, and J. K. Nørskov, *Electrochim. Acta* **48**, 3731 (2003).
- [12] B. Hammer, Y. Morikawa, and J. K. Nørskov, *Phys. Rev. Lett.* **76**, 2141 (1996).
- [13] B. Hammer and J. K. Nørskov, *Nature* **376**, 238 (1995).
- [14] J. K. Nørskov, T. Bligaard, A. Logadottir, S. Bahn, L. B. Hansen, M. Bollinger, H. Bengaard, B. Hammer, Z. Sljivancanin, M. Mavrikakis, et al., *J. Catal.* **209**, 275 (2002).
- [15] J. Greeley and M. Mavrikakis, *Nat. Mater.* **3**, 810 (2004).
- [16] K. Reuter, D. Frenkel, and M. Scheffler, *Phys. Rev. Lett.* **93**, 116105 (2004).
- [17] B. Hammer, L. B. Hansen, and J. K. Nørskov, *Phys. Rev. B* **59**, 7413 (1999).
- [18] P. J. Feibelman, B. Hammer, J. K. Nørskov, F. Wagner, M. Scheffler, R. Stumpf, R. Watwe, and J. Dumesic, *J. Phys. Chem. B* **105**, 4018 (2001).
- [19] M. Gajdoš and J. Hafner, *Surf. Sci.* **590**, 117 (2005).
- [20] L. Köhler and G. Kresse, *Phys. Rev. B* **70**, 165405 (2004).
- [21] G. Kresse, A. Gil, and P. Sautet, *Phys. Rev. B* **68**, 73401 (2003).
- [22] I. Grinberg, Y. Yourdshahyan, and A. M. Rappe, *J. Chem. Phys.* **117**, 2264 (2002).
- [23] S. E. Mason, I. Grinberg, and A. M. Rappe, *Phys. Rev. B* **69**, 161401 (2004).
- [24] H. Grönbeck, *Surf. Sci.* **559**, 214 (2004).
- [25] K. Doll, *Surf. Sci.* **573**, 464 (2004).
- [26] M. Neef and K. Doll, *Surf. Sci.* **600**, 1085 (2006).
- [27] X. Wu, M. C. Vargas, S. Nayak, V. Lotrich, and G. Scoles, *J. Chem. Phys.* **115**, 8748 (2001).
- [28] H. Orita, N. Itoh, and Y. Inada, *Chem. Phys. Lett.* **384**, 271 (2004).
- [29] R. A. Olsen, P. H. T. Philipsen, and E. J. Baerends, *J. Chem. Phys.* **119**, 4522 (2003).
- [30] M. Birgersson, C.-O. Almbladh, M. Borg, and J. N. Andersen, *Phys. Rev. B* **67**, 454020 (2003).
- [31] J. Greeley, A. A. Gokhale, J. Kreuser, J. A. Dumesic, H. Topsøe, N. Y. Topsøe, and M. Mavrikakis, *J. Catal.* **213**, 63 (2003).
- [32] M. Mavrikakis, J. Rempel, J. Greeley, L. B. Hansen, and J. K. Nørskov, *J. Chem. Phys.* **117**, 6737 (2002).
- [33] D. Vanderbilt, *Phys. Rev. B* **41**, 7892 (1990).
- [34] J. P. Perdew, K. Burke, and M. Ernzerhof, *Phys. Rev. Lett.* **77**, 3865 (1996).
- [35] N. Marzari, Ph.D. thesis, University of Cambridge (1996).
- [36] D. R. Lide, ed., *CRC Handbook of Chemistry and Physics* (Taylor and Francis, 2007), 88th ed.
- [37] C. Lu, I. C. Lee, R. I. Masel, A. Wieckowski, and C. Rice, *J. Phys. Chem. A* **106**, 3084 (2002).
- [38] D. F. Ogletree, M. A. Vanhove, and G. A. Somorjai, *Surf. Sci.* **173**, 351 (1986).
- [39] G. Q. Lu, J. O. White, and A. Wieckowski, *Surf. Sci.* **564**, 131 (2004).
- [40] H. Steininger, S. Lehwald, and H. Ibach, *Surf. Sci.* **123**, 264 (1982).
- [41] J. A. Steckel, A. Eichler, and J. Hafner, *Phys. Rev. B* **68**, 85416 (2003).
- [42] S. Baroni, S. de Gironcoli, A. Dal Corso, and P. Giannozzi, *Rev. Mod. Phys.* **73**, 515 (2001).
- [43] G. Blyholder, *J. Phys. Chem.* **68**, 2772 (1964).
- [44] A. Föhlisch, M. Nyberg, J. Hasselstrom, O. Karis, L. G. M. Pettersson, and A. Nilsson, *Phys. Rev. Lett.* **85**, 3309 (2000).

- [45] A. Zupan, K. Burke, M. Ernzerhof, and J. P. Perdew, *J. Chem. Phys.* **106**, 10184 (1997).
- [46] M. Gajdoš, A. Eichler, and J. Hafner, *J. Phys. Condens. Matter* **16**, 1141 (2004).
- [47] T. E. Shubina and M. T. M. Koper, *Electrochim. Acta* **47**, 3621 (2002).
- [48] B. C. Han and G. Ceder, *Phys. Rev. B* **74**, 205418 (2006).
- [49] A. Gil, A. Clotet, J. M. Ricart, G. Kresse, M. García-Hernández, N. Rosch, and P. Sautet, *Surf. Sci.* **530**, 71 (2003).
- [50] V. I. Anisimov, F. Aryasetiawan, and A. I. Lichtenstein, *J. Phys. Condens. Matter* **9**, 767 (1997).
- [51] M. Cococcioni and S. de Gironcoli, *Phys. Rev. B* **71**, 35105 (2005).
- [52] A. D. Becke, *J. Chem. Phys.* **98**, 5648 (1993).
- [53] A. B. Anderson and M. K. Awad, *J. Am. Chem. Soc.* **107**, 7854 (1985).
- [54] A. Dal Corso, *Phys. Rev. B* **64**, 235118 (2001).
- [55] K. Laasonen, A. Pasquarello, R. Car, C. Lee, and D. Vanderbilt, *Phys. Rev. B* **47**, 10142 (1993).